Journal of Alloys and Compounds 799 (2019) 563–572

Contents lists available at ScienceDirect

Journal of Alloys and Compounds

journal homepage: http://www.elsevier.com/locate/jalcom

Spin-phonon coupling in uniaxial anisotropic spin-glass based on Fe_2TiO_5 pseudobrookite

João E.F.S. Rodrigues [a, b, c, *], Washington S. Rosa [b], Mateus M. Ferrer [d], Thiago R. Cunha [b], Maximiliano Jesús Moreno Zapata [e], Julio R. Sambrano [f], José L. Martínez [a], Paulo S. Pizani [b], José A. Alonso [a], Antonio C. Hernandes [c], Renato V. Gonçalves [c, **]

[a] Instituto de Ciencia de Materiales de Madrid, Consejo Superior de Investigaciones Cientificas, Cantoblanco, E-28049 Madrid, Spain
[b] Department of Physics, Federal University of São Carlos, PO Box 676, 13565-905, São Carlos SP, Brazil
[c] São Carlos Institute of Physics, University of São Paulo, PO Box 369, 13560-970, São Carlos SP, Brazil
[d] Department of Physics, Federal University of Pelotas, 96160-000, Pelotas RS, Brazil
[e] Departamento de Física, Laboratório de Cristalografia, Universidade Federal de Minas Gerais, Av. Antônio Carlos 6627, Belo Horizonte MG, 31270-901, Brazil
[f] Modeling and Molecular Simulations Research Group, São Paulo State University, UNESP, 17033-360, Bauru SP, Brazil

ARTICLE INFO

Article history:
Received 5 November 2018
Received in revised form
7 May 2019
Accepted 29 May 2019
Available online 31 May 2019

Keywords:
Fe_2TiO_5
Anisotropic spin-glass
Spin-phonon coupling
Magnetoelectric
DFT phonon
Theoretical Raman

ABSTRACT

The ferric pseudobrookite is a rare example of uniaxial anisotropic spin-glass insulator, depicting a multiglass behavior and magnetoelectric coupling. Here, we present Raman spectroscopy results in order to elucidate the spin-phonon coupling in Fe_2TiO_5 for the first time. The experimental data are supported by computational simulations performed in view of density functional theory, which allowed us to assign the main Raman-active modes. Temperature-dependent phonon behavior exhibited anomalous evolution around 55 and 80–200 K, which was explained as successive coupling between lattice and spin configuration arising from spin freezing and short-range magnetic correlation, respectively. Arguments that the magnetoelectric effect in Fe_2TiO_5 is mediated by spin-phonon coupling are presented.

1. Introduction

Currently, there has been an expressive interest concerning the use of nanostructured ferric pseudobrookite (Fe_2TiO_5) for reactions of artificial photosynthesis, as a photoanode, in view of its adequate electronic and structural properties [1,2]. Several authors have argued that this iron titanate may overcome the well-known issues when narrow semiconductors are employed for separation and transportation of charge carriers induced by visible-light [1,3]. These problems are related to fast recombination of the photocarriers, as a result of the short diffusion path, and poor water oxidation kinetics in recognized materials, such as WO_3, $BiVO_4$, and Fe_2O_3 [4]. Other possible uses for this iron titanate include pigments for heat-resistant colorants or industrial paints [5,6], humidity sensor [7], thermoelectricity [8], and as magnetoelectric material operating close to room condition [9].

The ferric pseudobrookite presents an orthorhombic unit cell with *Ccmm* space group at ambient temperature (D_{2h}^{17} or #63), which is an interesting example of spin-glass insulator with uniaxial anisotropy [10,11]. Alternative settings use space groups *Cmcm* and *Bbmm* [12]. There are two glassy freezing transitions coupled by Dzyaloshinskii-Moriya (DM) interaction: the longitudinal at $T_{LF} \approx 55$ K [13], and the transverse at $T_{TF} \approx 9$ K [14]. It means that only short-range magnetic orders occur below freezing temperatures, although magnetic correlations at short-range can also persist until ambient conditions. A second glassy state was observed for the electric dipoles in the temperature interval 100–150 K, with a remnant polarization of 4000 $\mu C\,m^{-2}$ at 10 K in the absence of magnetic field [9]. These properties create a scenario containing both electric and magnetic short-range order and, then,

* Corresponding author. Instituto de Ciencia de Materiales de Madrid, Consejo Superior de Investigaciones Cientificas, Cantoblanco, E-28049 Madrid, Spain.
** Corresponding author.
E-mail addresses: rodrigues.joaoelias@df.ufscar.br (J.E.F.S. Rodrigues), rgoncalves@ifsc.usp.br (R.V. Gonçalves).

https://doi.org/10.1016/j.jallcom.2019.05.343
0925-8388/

defining the multiglass configuration in ferric pseudobrookite. It is also reported the magnetoelectric coupling that opens up opportunities for exploring this property in disordered magnetic materials [9,15].

In recent years, Raman spectroscopy became a complementary tool and important for probing magnetic order at long-range through the coupling between phonons and spins of the magnetic ions [16–19]: the spin-phonon coupling. In the absence of a structural phase transition of an insulator material, the coupling signatures take place when both position and linewidth depart from their expected behavior due to pure anharmonic effects in the vicinity of the magnetic transitions. Baltensperger and Helman showed that the phonon position below critical temperature will be dependent on the scalar spin correlation function [20–22]. Until now, little is known about spin-phonon coupling in systems depicting short-range magnetic order [23], except few works reporting coupling between lattice and magnetic short-range clusters [24–27]. Also, to the best of our knowledge, there are no investigations on the symmetry assignment of the optical modes in ferric pseudobrookite.

This work exploited the low temperature Raman spectra in a spin-glass insulator system viewing to elucidate the mechanisms of the magnetoelectric coupling in oxides containing short-range electric and magnetic order. As a candidate, we employed the uniaxial anisotropic spin-glass Fe_2TiO_5 with pseudobrookite crystal structure obtained by conventional solid-state method. Our Raman results were combined with X-ray powder diffraction, scanning electron microscopy, X-ray absorption near edge structure, X-ray photoelectron spectroscopy, and magnetic susceptibility data to better characterize the structural, morphological, compositional, and magnetic properties of the ferric pseudobrookite. This work may elucidate details on the coupling between magnetic and electric order in more general magnetoelectric materials [28].

2. Experimental methods

2.1. Synthesis and (micro)structural characterization

Polycrystalline Fe_2TiO_5 was synthesized by conventional solid-state reaction method, in which starting powders of Fe_2O_3 (99.5%, purchased from Sigma-Aldrich) and TiO_2 (99.5%, purchased from Sigma-Aldrich) were stoichiometrically weighted and mixed for 24 h with zirconia balls and isopropyl alcohol in nylon jar. The dry oxide mixtures were then double-calcined in air by two-steps at: (i) 1273 K for 4 h and (ii) 1373 K for 4 h. Final samples were further ground into fine powders. The phase purity and crystalline structure were probed by X-ray powder diffraction using a Rigaku diffractometer with Cu-$K\alpha$ radiation (40 *k*V, 30 mA) in 2θ interval $10°–140°$ (step size = 0.02°, step time = 10 s) and graphite monochromator. The diffraction pattern was compared with Card No. 88380 available at Inorganic Crystal Structure Database (ICSD, FIZ Karlsruhe and NIST). The Rietveld refinement was performed by using *FullProf* [29] program, in which the scale factor, offset, background, unit cell, Cagglioti parameters, atomic positions, isotropic atomic displacements, and occupation factors were adjusted. The formation of ferric pseudobrookite was confirmed without trace of Fe_2O_3 or TiO_2 as secondary phase. Morphological analysis was carried out in a Field emission scanning electron microscopy (FEG-SEM, model SIGMA, ZEISS), equipped with an energy dispersive X-ray spectrometer, showing some nearly cubic particles with average size of 0.8 μm. Details are available in Supporting Information.

2.2. Surface chemistry and X-ray absorption

For the surface investigations, X-ray photoelectron spectroscopy (XPS) at ambient temperature was performed in an *Omicron-Scienta* spectrometer, equipped with a monochromatic Al K_α X-rays. Surface charging was eliminated with an electron flood gun. The pass energy of the analyzer was held at 50 eV for both the survey and high resolution analysis. XPS spectra analysis was conducted with the *CasaXPS* software. The resulting spectra were corrected in energy with the C 1*s* peak (at 284.8 eV). Peak decomposition was achieved by using a Shirley baseline and applying Lorentzian and Gaussian functions curves with an asymmetric Voigt parameter. Local atomic structural studies were performed by X-ray absorption spectroscopy (XAS) measurements at the *XAFS2* beamline of the Brazilian Synchrotron Light Laboratory (LNLS–CNPEM, Campinas, Brazil). Measurements were performed using the Si(111) monochromator and three ionizing chambers were used for determining the photon flux before and after the sample and before and after a metal foil used as standard for energy calibration. Spectra analysis was conducted with the *IFEFFIT* library using the GUI Athena software [30].

2.3. Magnetic characterization

Magnetic properties by means of *ZFC-FC* magnetization vs. temperature curves (*ZFC* = Zero Field Cooled and *FC* = Field Cooled), in a DC field of 1 kOe, and AC susceptibility thermal spectra at 100 Hz, 500 Hz, 1 kHz, 5 kHz, and 10 kHz, with 10 Oe of AC field, were obtained in a commercial physical property measurement system (PPMS) by Quantum Design. The sample was placed in a residual vacuum of He atmosphere (pressure of 10^{-5} Torr), in the temperature range from 5 up to 300 K, collecting data at intervals of ~1 K.

2.4. Raman spectroscopy

Spin-phonon coupling was probed by taking Raman spectroscopy data, which were recorded in a *HR*800 Evolution spectrometer from Horiba *Jobin-Yvon*, equipped with a Peltier-cooled *CCD* detector, 600 and 1800 gr mm^{-1} diffraction gratings and Olympus microscope (50 × objective LD, NA = 0.35). As an excitation source, a helium-neon laser operating at 633 nm was used in quasi-backscattering geometry. At the sample's surface, the laser power was kept below of ~0.4 mW in order to avoid local overheating. A helium closed cycle cryostat with a temperature controller *Lake-Shore* 330 was used for the low temperature measurements (from 15 up to 275 ± 0.5 K) in high vacuum (10^{-6} mbar). The high temperature measurements (from 350 up to 500 ± 1 K) were performed with the sample inside a Linkan TS1500 micro-furnace. All the spectra were further corrected by the Bose-Einstein thermal factor prior to the fitting procedures by the Lorentzian functions [31], being it conducted within the *PeakFit* software.

3. Computational methods

The computational simulations were performed according to the periodic density functional theory (DFT) with *WC1LYP* hybrid functional [32] implemented on *CRYSTAL*17 program [33]. The choice of this functional was due to the better results on the electronic and structural parameters. Iron, titanium, and oxygen centers were described by 86-411d41G [34], 8-6411(31d)g [35], and 8-411(1d)G all-electron basis sets, respectively. The calculations were conducted with truncation criteria for the Coulomb and exchange series controlled by a set of five thresholds (10^{-8}, 10^{-8}, 10^{-8}, 10^{-8}, and 10^{-16}), and shrinking factors set to 8 for Pack-Monkhorst and Gilat net. The convergence was achieved by setting in 2 the difference between the number of α and β electrons of the first five Self-Consistent Field (SCF) cycles. The initial atomic positions and

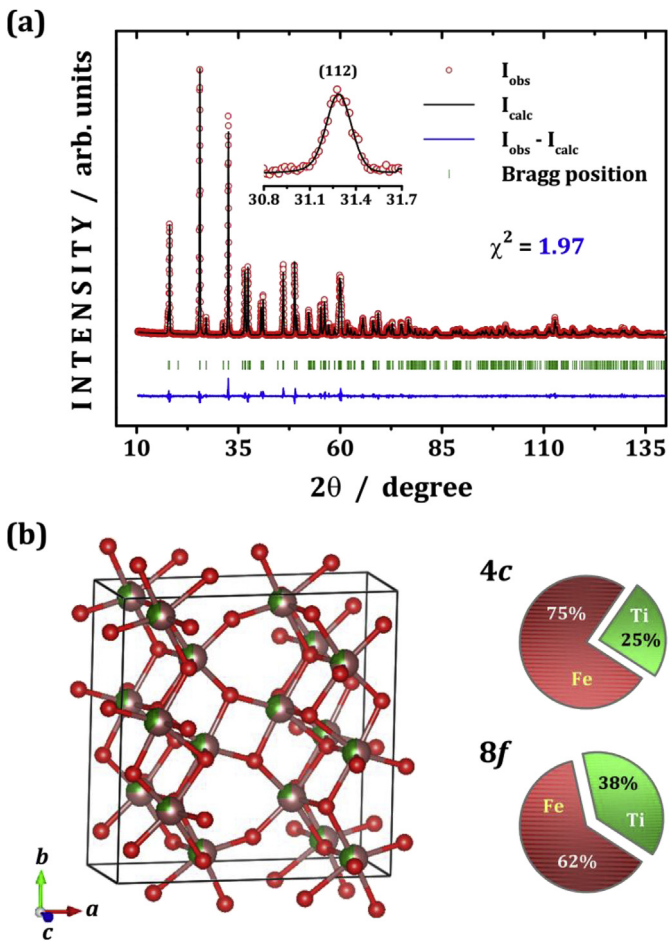

Fig. 1. (a) X-ray powder diffraction (XRPD) data for Fe_2TiO_5 pseudobrookite. The red open circles indicate the experimental data, the black line the refined data, the blue line the difference between experimental and refined data, and the green markers the Bragg positions. (b) Schematic representation of the pseudobrookite crystal structure with the *VESTA* software. (For interpretation of the references to color in this figure legend, the reader is referred to the Web version of this article.)

lattice parameters were set according to the ICSD Card No. 24134. All the Raman modes were calculated by means of numerical second derivatives of the total energy. The Raman intensities were calculated by the CPHF/KS scheme [36,37].

4. Results and discussion

From X-ray data and Rietveld refinement in Fig. 1(a), it was confirmed that the as-synthesized ferric pseudobrookite belongs to the orthorhombic *Bbmm* space group (D_{2h}^{17} or #63) with four formulas per unit cell ($Z = 4$). The refined parameters including lattice constants, atomic positions, occupancies, and atomic displacements are summarized in Table 1. At this point, it is worth discussing some crystal structure details on the Fe_2TiO_5. A debate in literature was started after the earlier results of Linus Pauling concerning the orthorhombic phase of ferric pseudobrookite [38]. A first structural solution was reported by Wyckoff, which considered a fully ordered structure with Fe^{3+} at 8*f* (M_{8f}) and Ti^{4+} at 4*c* (M_{4c}) sites, within the D_{2h}^{17} space group. These two sites are represented in Fig. 1(b), which depicts a network of M_{8f} and M_{4c} octahedra. More careful analyses have shown that both nonequivalent sites are shared by Fe^{3+} and Ti^{4+} cations (partial occupancy) with a slightly preferential tendency of iron (titanium) at 4*c* (8*f*) positions [5,12].

Indeed, from the refinement, the iron ions occupy ~75% of 4*c* sites, while these ions are in ~62% of 8*f* positions. It means that our pseudobrookite is different from fully disordered structure, in which iron ions are in ~67% and ~67% of 4*c* and 8*f* sites, respectively. This assumption is also confirmed by the occurrence of (112) reflection peak at $2\theta \simeq 31.3^\circ$ [12]. Table 2 displays the most representative interatomic distances and angles. It is clear that the 8*f* sites show a strong distortion when compared to 4*c* ones. The bond distance data also provided information on the iron and titanium valence states by means of Bond Valence Sum (BVS), confirming the presence of Fe^{3+} and Ti^{4+} cations. As reported by Atzmony et al., the spin-glass behavior in ferric pseudobrookite is a direct consequence of the cation distribution on 8*f* and 4*c* sites, leading to a random spin canting and, consequently, the spin-glass freezing [39].

The local atomic feature of the as-synthesized ferric pseudobrookite was investigated by XANES technique. The Ti *K*-edge XANES spectrum in Fig. 2(a) displays a well-resolved pre-edge peak at 4971 eV that is attributed to Ti dipolar electronic transition ($1s \longrightarrow 3d$). This pre-edge peak also means that the Ti^{4+} cations are present on the structure of the pseudobrookite. The shape of this pre-edge peak is different compared with TiO_2 (anatase or rutile phases) [40], but very similar to that previously reported for Fe_2TiO_5 [40]. For the Fe *K*-edge XANES spectrum in Fig. 2(b), the pre-edge peak located at 7114 eV can be associated with Fe^{3+} cations from the Fe_2TiO_5 stoichiometry.

The chemical surface composition of the as-synthesized ferric pseudobrookite was probed by XPS technique. The XPS Ti 2*p* spectrum in Fig. 2(c) depicts two photoelectron peaks centered at binding energies of 458.4 (Ti $2p_{3/2}$) and 464.2 eV (Ti $2p_{1/2}$), which are ascribed to the presence of the Ti^{4+} cations in the Fe_2TiO_5 system. The Fe 2*p* spectrum in Fig. 2(d) shows the occurrence of two peaks located at 711.1 and 724.8 eV, which are associated with Fe $2p_{3/2}$ and Fe $2p_{1/2}$ photoemissions, respectively. A satellite peak is clearly visible at 718.9 eV, which attested the presence of Fe^{3+} ions [41]. Both XANES and XPS results are in good agreement with

Table 1
Structural parameters of the Fe_2TiO_5 pseudobrookite at room temperature obtained in the Rietveld refinement (Space group: *Bbmm* or #63).

Atom	Wyckoff site	*x*	*y*	*z*	U_{iso} (Å^2)	Occupancy
Fe1/Ti1	4*c*	0.1875(1)	0.25000	0.00000	0.0029(2)	0.76(2)/0.24(2)
Fe2/Ti2	8*f*	0.13582(7)	0.56402(7)	0.00000	0.003(1)	0.624(9)/0.376(9)
O1	4*c*	0.7581(6)	0.25000	0.00000	0.0053(7)	1.000
O2	8*f*	0.0477(3)	0.1164(3)	0.00000	0.0037(5)	1.000
O3	8*f*	0.3116(3)	0.0717(3)	0.00000	0.0026(4)	1.000
Unit cell parameters		**Cagglioti parameters**		**Reliability factors**		
a (Å)	9.7882(1)	*U*	0.0413(2)	R_p (%)	11.60	
b (Å)	9.9770(2)	*V*	−0.0373(2)	R_{wp} (%)	15.10	
c (Å)	3.72993(5)	*W*	0.03618(7)	R_{exp} (%)	10.78	
V (Å^3)	364.25(1)	Shape	0.4161(6)	R_{Bragg} (%)	4.430	
ρ (g.cm^{-3})	4.371			χ^2	1.970	

Table 2
Interatomic distances and angles obtained in the Rietveld refinement of the XRPD pattern. Bond Valence Sum (BVS) for iron and titanium is also provided.

M_{4c} ≡ (Fe1,Ti1)		M_{8f} ≡ (Fe2,Ti2)	
Bond	*Distance* (Å)	*Bond*	*Distance* (Å)
M_{4c}–O1 (×2)	1.989(2)	M_{8f}–O1 (×1)	2.126(3)
M_{4c}–O2 (×2)	1.911(3)	M_{8f}–O2 (×1)	1.871(3)
M_{4c}–O3 (×2)	2.154(3)	M_{8f}–O2 (×1)	1.996(3)
		M_{8f}–O3 (×2)	1.9362(8)
		M_{8f}–O3 (×1)	2.190(3)
⟨M_{4c}–O⟩	2.018	⟨M_{8f}–O⟩	2.009
BVS (Fe1)	3.09(1)	BVS (Fe2)	3.19(1)
BVS (Ti1)	3.60(1)	BVS (Ti2)	3.71(1)
O–M_{4c}–O angles		O–M_{8f}–O angles	
Angle	(°)	*Angle*	(°)
O1–M_{4c}–O2 (×4)	104.4(2)	O1–M_{8f}–O2 (×1)	103.0(3)
O1–M_{4c}–O3 (×4)	78.8(1).	O1–M_{8f}–O2 (×1)	176.4(3)
O2–M_{4c}–O3 (×2)	80.1(2)	O1–M_{8f}–O3 (×2)	80.5(1)
O2–M_{4c}–O3 (×2)	168.6(3)	O1–M_{8f}–O3 (×1)	99.0(2)
		O2–M_{8f}–O3 (×1)	77.4(2)
		O2–M_{8f}–O3 (×2)	98.7(2)
		O2–M_{8f}–O3 (×2)	104.1 (2)
		O2–M_{8f}–O3 (×1)	158.0(3)
M_{4c}–O–M_{8f} angles			
Angle		(°)	
M_{4c}–O1–M_{8f} (×4)		99.8(1)	
M_{4c}–O2–M_{8f} (×1)		108.6(1)	
M_{4c}–O2–M_{8f} (×1)		152.0(1)	
M_{4c}–O3–M_{8f} (×1)		93.9(1)	
M_{4c}–O3–M_{8f} (×2)		100.52(9)	

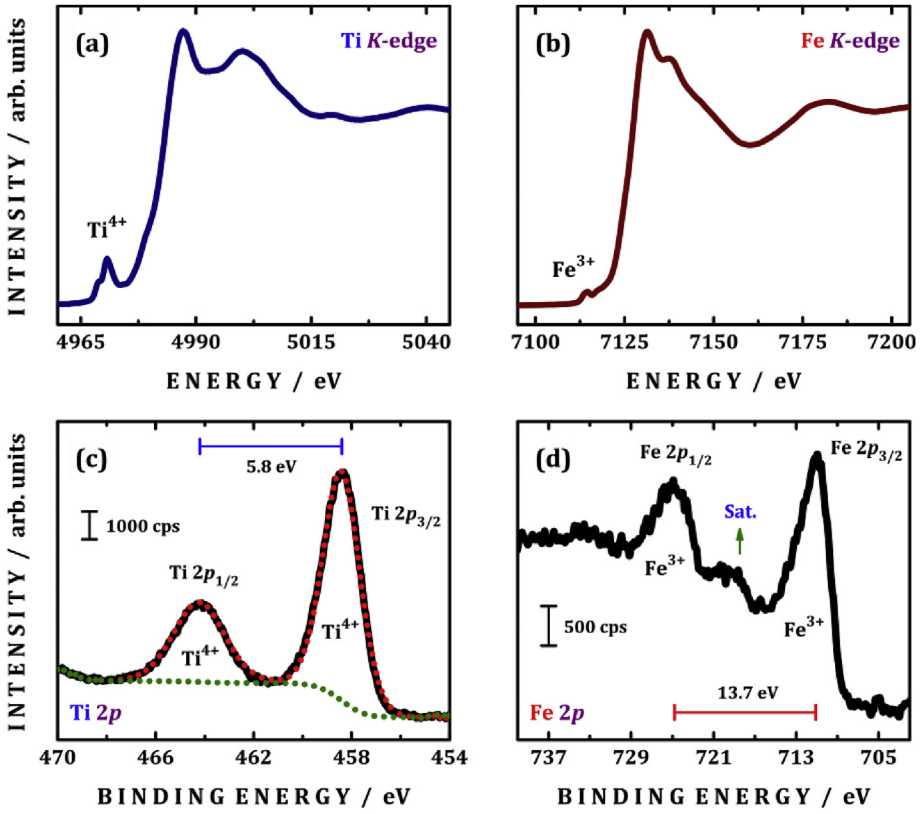

Fig. 2. (a) Ti *K*-edge XANES spectrum, (b) Fe *K*-edge XANES spectrum, (c) Ti 2*p* XPS spectrum, and (d) Fe 2*p* XPS spectrum for the as-prepared ferric pseudobrookite. Both techniques showed the occurrence of iron and titanium cations with valence states of 3 + and 4+, respectively. In (c), the dotted lines (red and green) are the fitted data and Shirley-type baseline function, respectively. (For interpretation of the references to color in this figure legend, the reader is referred to the Web version of this article.)

X-ray data in view of the BVS summation, indicating that the solid-state reaction was successful to synthesize ferric pseudobrookite.

Fig. 3 depicts the DC and AC magnetization behavior as a function of temperature in the interval between 5 and 100 K. For completeness, we confirmed reported results [9,10,42] on the magnetic properties of Fe_2TiO_5 pseudobrookite, mainly focusing on the spin-glass phenomena. In the *ZFC* curve with 1 kOe of applied field, a χ_{DC}-peak at 55 K should be ascribed to the longitudinal freezing transition (T_{LF}), while a second broad maximum located at 9 K is a signature of the transverse freezing transition (T_{TF}). The first signature of the spin-glass character of Fe_2TiO_5 pseudobrookite comes from the bifurcation of *ZFC-FC* curves below T_{LF}, which is related to the irreversible feature depicted by spin-glass materials. The second signature may be seen through the AC susceptibility data in a field of 10 Oe. Particularly, both χ'_{AC}- and χ''_{AC}-peaks at T_{LF} are frequency-dependent and shifting for increased frequency, as shown in details of Fig. 3. Our results are in good agreement with other magnetic investigations performed on the single crystal and powder forms of ferric pseudobrookite, confirming its spin-glass character and the partial occupancy of 8*f* and 4*c* crystallographic sites.

Based on the site distribution in Guo et al. [12], the number and symmetry of optical phonons at the Brillouin zone-center (Γ-point) was calculated by taking the irreducible representation of D_{2h} factor group, as summed up in last column of Table 3. The phonons with infrared and Raman responses are foreseen as 18 IR-active ($\Gamma_{IR} = 7\mathbf{B}_{1u} \oplus 4\mathbf{B}_{2u} \oplus 7\mathbf{B}_{3u}$) and 24 Raman-active ($\Gamma_{Raman} = 8\mathbf{A}_g \oplus 5\mathbf{B}_{1g} \oplus 8\mathbf{B}_{2g} \oplus 3\mathbf{B}_{3g}$) modes. Here, *g* and *u* subscripts represent the parity under the inversion symmetry, which sets the mutual exclusion rule of states in centrosymmetric crystal structures. Raman spectra at 15 K were acquired in ferric pseudobrookite, as summarized in Fig. 4. Since one should expect 24 Raman modes in the first-order spectra, it was carried out a carefully spectral decomposition by Lorentzian functions. It can be seen that only 21 bands are defined to be clearly identified through the fitting analysis. It is also important to highlight that no signals of anatase (143 cm^{-1}) [43], rutile (442 and 609 cm^{-1}) [44,45], or hematite (1310 cm^{-1}) [46] phases were found, corroborating that our ferric pseudobrookite samples are free of spurious phases. Also, the distribution of main Raman modes in Fig. 4 is in accordance with other reported results [47,48].

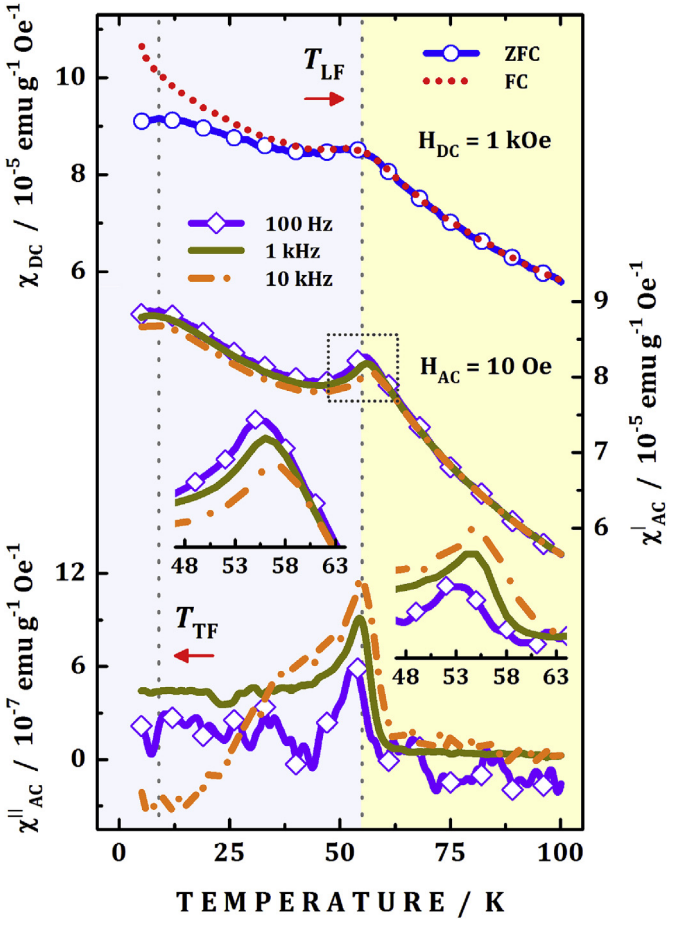

Fig. 3. Temperature dependence of the magnetic susceptibility (χ) thermal spectra for the Fe_2TiO_5 pseudobrookite. *Top-row*: DC magnetization (*ZFC* and *FC*) as a function of temperature. *Bottom-row*: AC susceptibility thermal spectra at some representative frequencies, namely 100 Hz, 1 kHz, and 10 kHz.

In literature, to our knowledge, there are no papers devoted to assign the vibrational modes of ferric pseudobrookite. However, Bersani et al. reported the Raman spectrum of natural pseudobrookites in order to be employed as a reference [47]. Wang et al. extracted the ferric pseudobrookite Raman spectra in yellow zones of marbled sigillata, arguing that this phase was stabilized by partial cationic disorder due to the Al and/or Mg substitutions into the crystal structure [48]. Based on the force constant calculations for the anatase and brookite phases, they attributed the bands at 200–220 cm^{-1} (Peaks No 5 and 6, in Fig. 4), in Raman spectra of Fe_2TiO_5, to the bending-type motions, while that one at 660 cm^{-1} (Peak No 17, in Fig. 4) to the stretching-type vibrations. Such modes are sensitive to the disorder effect allowing its monitoring through line broadening.

In this work, the Raman spectrum of ferric pseudobrookite was calculated by means of density functional theory method. The accordance between experimental and theoretical data was partially reached in view of the mode position, as shown in Fig. S2 of *Supporting Information*. Since we have employed an ordered primitive unit cell, i.e. without partial site occupation, for calculations, one can conclude that our synthesized Fe_2TiO_5 has some degree of cationic disorder, as confirmed by Rietveld refinement in Table 1. This assumption is in accordance with the work of He et al. on the lattice dynamics in pseudobrookite-type $MgTi_2O_5$ [49]. The authors optimized a fully ordered pseudobrookite to extract its optical modes, which showed a good agreement with experimental data. The main reason for that was the high degree of cationic order achieved after annealing process. Even so, the main bands in Fig. 4 are tentatively assigned in Table 4. Fig. 5 displays the atomic displacement patterns for some selected Raman active modes in Fe_2TiO_5 pseudobrookite. The low wavenumber modes below 200 cm^{-1} are mainly related to displacements of M_{4c} and oxygens anions in M_{4c}–$(O)_4$ units, as described by the primitive unit cell for the phonon calculation. The intermediate modes at 250–400 cm^{-1} mainly concern movements arising from M_{8f} and M_{4c} sites, which include polar displacements, stretching, and bending of O–$(M_{8f})_2$ and M_{4c}–$(O)_4$ units. Besides, out-of-plane plane oxygen bending in M_{4c}–$(O)_4$ units has energy near 661 cm^{-1} (calc. 651 cm^{-1}), while the $\mathbf{A}_g$ mode at 787 cm^{-1} (calc. 809 cm^{-1}) represents symmetric oxygen stretching. In the partially disordered state, these modes involve iron ions, being also affected by changes in M_{8f}–O and M_{4c}–O bond lengths. The complete set of the vibrational patterns for all the $\mathbf{A}_g$, $\mathbf{B}_{1g}$, $\mathbf{B}_{2g}$, and $\mathbf{B}_{3g}$ symmetries can be found in *Supporting Information*.

Spin-phonon coupling was probed by following the trend of the Raman modes near critical temperature at 55 K, corresponding to the longitudinal freezing transition (T_{LF}), and also for temperatures well above T_{LF}, in which the Fe_2TiO_5 pseudobrookite depicts magnetoelectric coupling. Fig. 6 exhibits the temperature-dependent Raman spectra of Fe_2TiO_5 pseudobrookite in the

Table 3
Nuclear site group analysis for the ferric pseudobrookite (Fe_2TiO_5) with orthorhombic unit cell belonging to the Ccmm space group.

Atom	Site	Symmetry	Irreducible Representation
Fe1/Ti1	4*c*	C_{2v}^{x} (2 *mm*)	$\mathbf{A}_g \oplus \mathbf{B}_{1g} \oplus \mathbf{B}_{2g} \oplus \mathbf{B}_{1u} \oplus \mathbf{B}_{2u} \oplus \mathbf{B}_{3u}$
Fe2/Ti2	8*f*	C_{S}^{xz} (.*m*.)	$2\mathbf{A}_g \oplus \mathbf{B}_{1g} \oplus 2\mathbf{B}_{2g} \oplus \mathbf{B}_{3g} \oplus \mathbf{A}_u \oplus 2\mathbf{B}_{1u} \oplus \mathbf{B}_{2u} \oplus 2\mathbf{B}_{3u}$
O1	4*c*	C_{2v}^{x} (2 *mm*)	$\mathbf{A}_g \oplus \mathbf{B}_{1g} \oplus \mathbf{B}_{2g} \oplus \mathbf{B}_{1u} \oplus \mathbf{B}_{2u} \oplus \mathbf{B}_{3u}$
O2	8*f*	C_{S}^{xz} (.*m*.)	$2\mathbf{A}_g \oplus \mathbf{B}_{1g} \oplus 2\mathbf{B}_{2g} \oplus \mathbf{B}_{3g} \oplus \mathbf{A}_u \oplus 2\mathbf{B}_{1u} \oplus \mathbf{B}_{2u} \oplus 2\mathbf{B}_{3u}$
O3	8*f*	C_{S}^{xz} (.*m*.)	$2\mathbf{A}_g \oplus \mathbf{B}_{1g} \oplus 2\mathbf{B}_{2g} \oplus \mathbf{B}_{3g} \oplus \mathbf{A}_u \oplus 2\mathbf{B}_{1u} \oplus \mathbf{B}_{2u} \oplus 2\mathbf{B}_{3u}$
		Total	$8\mathbf{A}_g \oplus 5\mathbf{B}_{1g} \oplus 8\mathbf{B}_{2g} \oplus 3\mathbf{B}_{3g} \oplus 3\mathbf{A}_u \oplus 8\mathbf{B}_{1u} \oplus 5\mathbf{B}_{2u} \oplus 8\mathbf{B}_{3u}$
		Acoustic	$\mathbf{B}_{1u} \oplus \mathbf{B}_{2u} \oplus \mathbf{B}_{3u}$
		Silent	$3\mathbf{A}_u$
		Infrared	$7\mathbf{B}_{1u} \oplus 4\mathbf{B}_{2u} \oplus 7\mathbf{B}_{3u}$
		Raman	$8\mathbf{A}_g \oplus 5\mathbf{B}_{1g} \oplus 8\mathbf{B}_{2g} \oplus 3\mathbf{B}_{3g}$

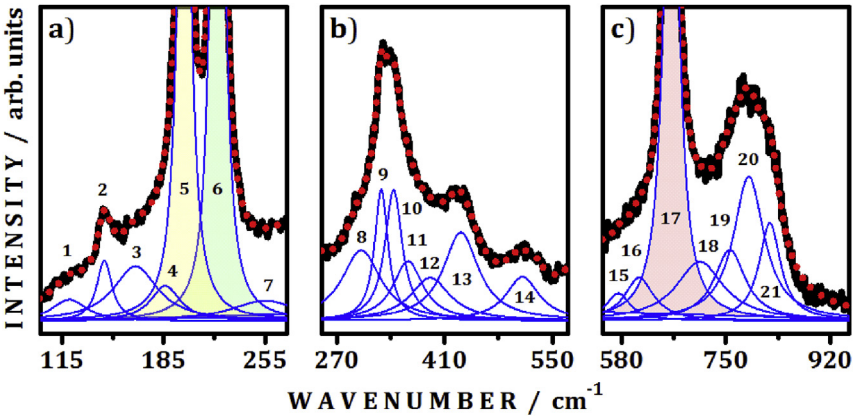

Fig. 4. Raman spectrum recorded at 15 K in ferric pseudobrookite and its spectral decomposition process, where black and dotted red lines are the experimental and fitted data, respectively. Blue lines represent Lorentzian profile functions. Both position Ω and width Γ of each mode is listed in Table S2 of *Supporting Information*. (For interpretation of the references to color in this figure legend, the reader is referred to the Web version of this article.)

Table 4
Assignment of the main Raman-active modes observed at 15 K in ferric pseudobrookite (Fe_2TiO_5).

Expt. at 15 K	DFT	Symmetry	Main atomic motion
144 (# 2)	144	$\mathbf{B}_{1g}$	M_{4c} and oxygens out-of-plane displacement in M_{4c}–$(O)_4$
199 (# 5)	211	$\mathbf{A}_g$	M_{4c} and oxygens in-plane displacement in M_{4c}–$(O)_4$
222 (# 6)	263	$\mathbf{B}_{1g}$	M_{8f} and oxygen out-of-plane motion in O–$(M_{8f})_2$ / M_{4c} polar motion in M_{4c}–$(O)_4$
327 (# 9)	364	$\mathbf{A}_g$	Symmetric stretching of O–$(M_{8f})_2$ / In-plane oxygen bending of M_{4c}–$(O)_4$
661 (#17)	651	$\mathbf{B}_{1g}$	Out-of-plane plane oxygen bending of M_{4c}–$(O)_4$
787 (#20)	809	$\mathbf{A}_g$	Symmetric oxygen stretching of M_{4c}–$(O)_4$

temperature interval 15–500 K. These spectra do not show signals of any structural phase transition close to the critical temperature, since the distribution of modes was maintained under temperature scanning. In the Balkanski description of the temperature-induced anharmonicity effects on the phonon position (Ω, in unit of cm^{-1}) [50], it can be expected a low temperature plateau followed by a negative linear decrease at high temperatures. The full mathematical expression for such a physical effect is given by the equation below:

$$\Omega(T) = \Omega(0) + C\left[1 + \frac{2}{e^{x} - 1}\right] + D\left[1 + \frac{3}{e^{y} - 1} + \frac{3}{(e^{y} - 1)^{2}}\right], \quad (1)$$

where $x = hc\Omega(0)/2k_BT$ and $y = hc\Omega(0)/3k_BT$; $\Omega(0)$, C and D (in units of cm^{-1}) are fitted parameters; h, c, k_B, and T maintain their usual meaning. Such a description includes both three- and four-phonon process for the perturbation analysis of the vibrational Hamiltonian [50].

Different from the expected, some interesting phenomena can be seen through the temperature dependence of the phonon position of the main bands at 199 ($\mathbf{A}_g$), 222 ($\mathbf{B}_{1g}$), and 661 ($\mathbf{B}_{1g}$) cm^{-1}, as depicted in Fig. 7(a–c). The phonons in ferric pseudobrookite do not follow the universal trend described by the Balkanski theory. Instead, they presented anomalies in two temperature intervals: 15–60 and 80–200 K. As earlier mentioned, the first region covers the longitudinal glassy freezing temperature related to the spin-glass behavior, while the second one includes the glassy trend for the electric dipoles. As argued by Sharma et al. [9], the electric polarization at 150 K (i.e. well above T_{LF}) and its dependence on applied magnetic field are evidences for the magnetoelectric coupling in Fe_2TiO_5. The origin of this property arises from the short-range magnetic correlations, which were first detected in neutron diffraction experiments performed by Atzmony et al. [10].

In the absence of a structural phase transition, the unit cell volume variation induced by temperature change is not enough to account the phonon anomalies, which induced the deviation from the pure anharmonic contribution. Previous investigations based on neutron diffraction, elastic, and specific heat measurements were not able to detect any anomalous trend near critical

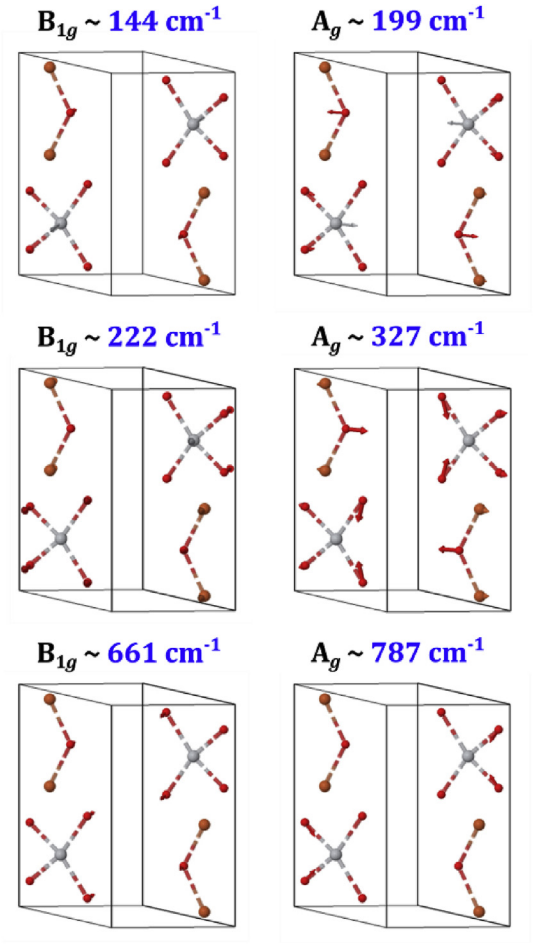

Fig. 5. Schematic representation of the main Raman modes listed in Table 4. Brown, gray, and red spheres in sketch of atomic motion represent iron (at M_{8f} sites), titanium (at M_{4c} sites) and oxygen atoms, respectively. The box represents the primitive unit cell employed for the phonon calculation. The vibrational patterns were interpreted in terms of the M_{4c}–$(O)_4$ and O–$(M_{8f})_2$ units. (For interpretation of the references to color in this figure legend, the reader is referred to the Web version of this article.)

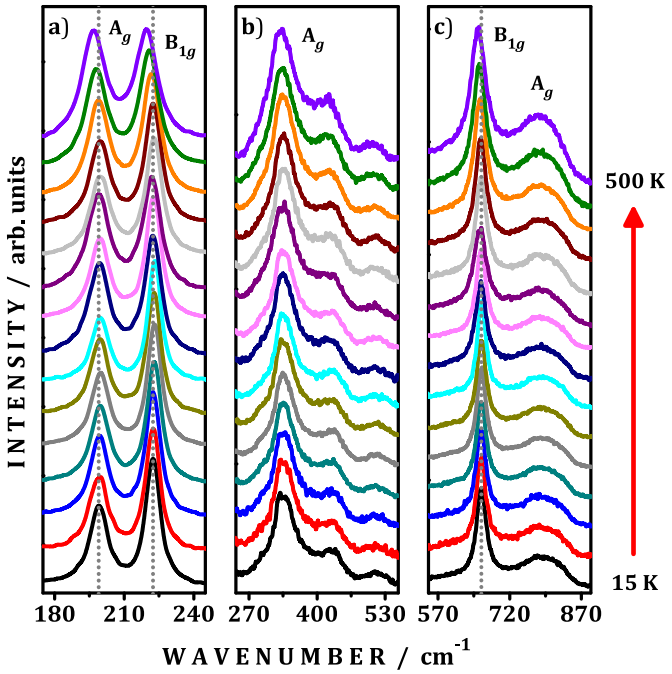

Fig. 6. Temperature-dependent Raman spectra of Fe_2TiO_5 between 15 and 500 K. There is no evidence for structural phase transition in this temperature interval, since the band distribution was kept the same for all the experiment.

temperature [10]. Then, we may ascribe such anomalies to magnetostriction or to spin-phonon coupling-induced phonon renormalization. Based on Fig. 7(d and e), which shows the temperature dependence of the linewidth (Γ, in units of cm^{-1}), the former attribution should be ruled out here, because the widths are not sensitive to magnetostriction effects [51,52] and, then, they should follow the Balkanski model [50] (at low *T*, linewidth approaches to a constant and, at high *T*, it increases monotonically). Instead, it can be noticed a cusp near to $T_{LF} \approx 55$ K in temperature-dependent linewidth, besides a broad minimum in the interval from 80 to 200 K. We should also discard possible electron-phonon coupling and its role in linewidth variation, once ferric pseudo-brookites are highly insulators at low temperature [9,15].

In this way, the anomalies observed in phonon position and linewidth are strong evidences for the spin-phonon coupling in Fe_2TiO_5. In particular, such a coupling occurs between lattice and spin configuration below T_{LF} (i.e. spin-glass-like freezing), which denotes the possibility of characterizing spin-glass behavior using inelastic light scattering spectroscopy. Above T_{LF}, instead, the coupling is modulated by phonons and short-range magnetic correlations, which may persist until ambient temperature [53]. Indeed, Sharma et al. [9] confirmed the correlation between real part of dielectric constant (ε) of pseudobrookite and scalar spin correlation function $\langle S_i \cdot S_j \rangle$, as described by the phenomenological model by Katsufuji and Takagi [54]:

$$\varepsilon = \varepsilon_0 \left[1 + \alpha \langle S_i \cdot S_j \rangle\right], \tag{2}$$

where *S* is the spin operator. The above result elucidates that the magnetoelectric effect in Fe_2TiO_5 well above T_{LF} is related to the spin-phonon interaction. More precisely, the magnetic correlations at short-range induces electric polarization variations, which affect the phonon position and, therefore, the dielectric constant [55].

Anomalous behavior and phonon softening or hardening close and below the magnetic ordering temperature are well documented phenomena in insulators with long-range magnetic order [22,56,57]. Such processes can be understood as a variation in exchange integral J_{ij} due to lattice vibration, which involves the relative displacements u_k^{α} of the pure lattice against the sublattice with magnetic ions [20,21]. In this sense, the energy of the magnetic sublattice can be evaluated for the nearest-neighbors, as follows:

$$H_m \approx -\sum_{i,j>i} J_{ij} \langle S_i \cdot S_j \rangle, \tag{3}$$

such that the summation covers the first-neighbors ions *j* around the *i*th iron ion. Considering the modulation of the exchange integral by αth Raman phonon, the calculation of the phonon energy should include the spin term, which accounts the shift in phonon position [56], i.e.

$$\Delta\Omega_{sp-ph} = \frac{1}{2\mu_\alpha \Omega_\alpha} \sum_k \hat{u}_k^{\alpha} \overline{D}_s \hat{u}_k^{\alpha}, \tag{4}$$

in which μ_α is the reduced mass, Ω_α denotes the αth phonon frequency, and $\overline{D}_s$ is the dynamic spin tensor, which has second derivatives of the exchange integral. Then, the development of Eq (4)

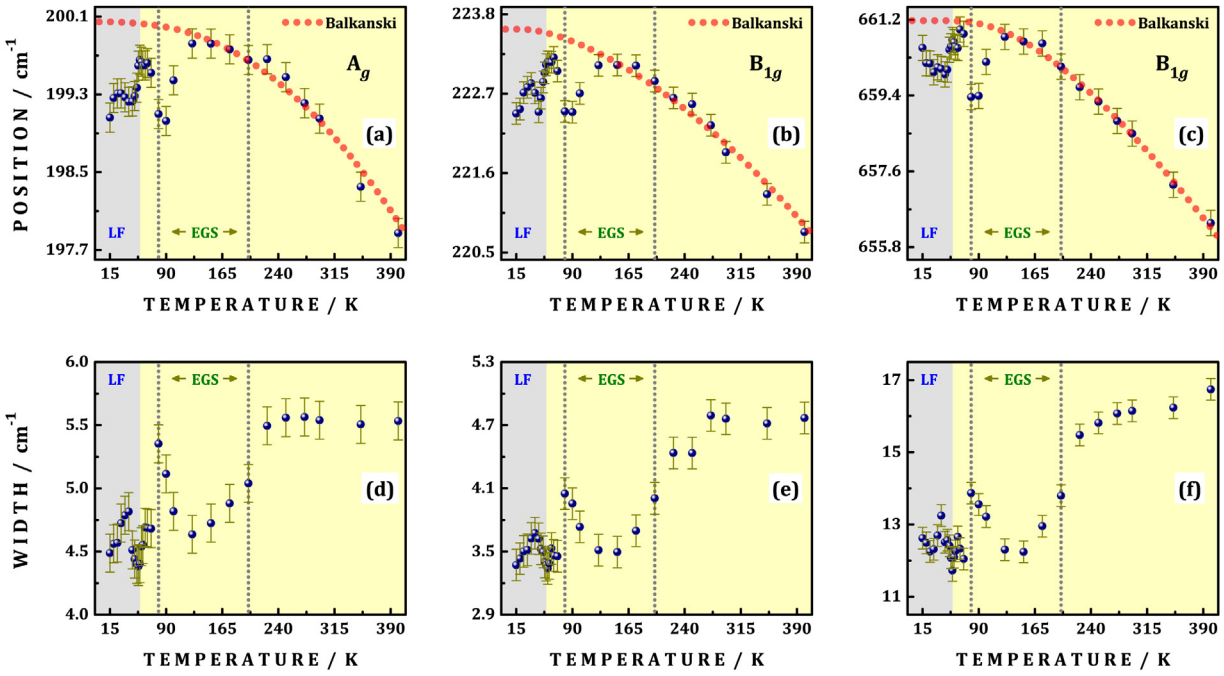

Fig. 7. Temperature dependence of the phonon position (*top-row*) (a–c) and linewidth (*bottom-row*) (d–f) of more representative Raman active modes of ferric pseudobrookite (Fe_2TiO_5). Dotted red lines represent the anharmonic contribution to the phonon position in view of the Balkanski theory. *Abbreviation*: LF = longitudinal freezing and EGS = electric-glass state. (For interpretation of the references to color in this figure legend, the reader is referred to the Web version of this article.)

will lead to the following equation: $\Delta\Omega_{sp-ph} = \lambda\langle S_i \cdot S_j\rangle$, where λ is the spin-phonon coupling coefficient, which may be different for each mode, taking positive or negative values. Better description of such a coefficient is done in view of the microscopy theory [21,58].

Based on the model earlier described, we may consider two temperature regimes for the spin-phonon coupling, once it were clearly observed two softening behavior at $T \lesssim T_{LF}$ (LF, longitudinal freezing) and at $80 \lesssim T \lesssim 200$ K (EGS, electric-glass state). Since the atomic motion u_k^α in each Raman active mode (e.g. stretching and bending vibrations) is not modified at both temperature intervals, we may consider that the reasons for different shift $\Delta\Omega_{sp-ph}$ values observed in Fig. 7(a–c) comes from modifications in both spin-phonon coupling coefficient and scalar spin correlation function. Indeed, λ value not only depends on mass and phonon frequency, but also on the exchange integral and its derivatives. At the same time, the spin correlation function will be sensitive to variations in the spin-spin interaction [11], since it is averaged over the spin system and opposite sublattice [20]. Both facts may explain two softening in our Raman data, representing successive spin-phonon couplings due to spin freezing and short-range magnetic correlation, respectively. The above results elucidates that the spin-phonon coupling plays a role in magnetoelectric property, which was attributed to the short-range magnetic correlations, well above T_{LF}, in view of the Katsufuji and Takagi model in Eq (2).

In literature, some recent papers have shown the capabilities of the Raman spectroscopy for detecting the magnetic order at short-range in oxide materials. Barbosa and Paschoal reported phonon softening above ambient temperature in partially ordered La_2NiMnO_6 perovskite, which was attributed to short-range interactions from ferromagnetic clusters of Ni^{3+}/Mn^{3+} embedded in a paramagnetic ordered lattice containing Ni^{2+} and Mn^{4+} cations [24]. Chakraborty et al. detected anomalous phonon behavior near to critical temperature in spin-glass $Y_{0.7}Tb_{0.3}MnO_3$ perovskite [25], confirming that the spin-phonon coupling should occur even in materials with local magnetic ordering. Milosavljević et al. observed a strong spin-lattice interaction related to short-range magnetic correlations in $CrSiTe_3$ trichalcogenide [27]. These results are not so surprising because Raman technique is a recognized tool employed to detect local disorder [59–63] and, then, the modulation in exchange integral by Raman active phonons will be also seen in systems containing only short-range magnetic order. Therefore, future studies are now encouraged to theoretically describe the spin-phonon interactions in magnetically short-range ordered compounds, as the case of Fe_2TiO_5 pseudobrookite.

5. Conclusion

In summary, we investigated the temperature-dependent Raman spectra of the ferric pseudobrookite between 15 and 500 K. No spectral variation induced by structural phase transition was detected during the temperature scanning. Our results elucidated that the anomalous phonon behaviors are strong evidences for the coupling between lattice and spin configuration arising from spin freezing ($T \lesssim T_{LF}$, the longitudinal freezing transition temperature) and short-range magnetic correlation well above T_{LF}. It means that the Raman scattering is able to probe spin-coupling effect in insulators with short-range magnetic order.

Acknowledgments

We thank the Brazilian agencies FAPESP (Proc. Numbers: 2013/07793-6, 2013/07296-2, and 2017/18716-3), CNPq (Proc. Number: 150936/2017-6), CAPES (Proc. Number: 88881.171031/2018-01 and 88887.166861/2018-00), and FAPEMIG for the financial support and the Brazilian Synchrotron Light Laboratory (Campinas SP, Brazil) for X-ray absorption spectroscopy measurements (Proposal Number: 20170832). JAA and JLM thank Spanish MINECO for funding the Project MAT2017-84496-R.

Appendix A. Supplementary data

Supplementary data to this article can be found online at https://doi.org/10.1016/j.jallcom.2019.05.343.

References

[1] Q. Liu, J. He, T. Yao, Z. Sun, W. Cheng, S. He, et al., Aligned Fe_2TiO_5-containing nanotube arrays with low onset potential for visible-light water oxidation, Nat. Commun. 5 (2014) 5122.

[2] L. Jin, C. Zhou, Electronic structures and optic properties of Fe_2TiO_5 using LSDA+U approach, Prog. Nat. Sci. Mater. Int. 23 (2013) 413–419.

[3] M. Wang, X. Wu, K. Huang, Y. Sun, Y. Zhang, H. Zhang, et al., Enhanced solar water-splitting activity of novel nanostructured Fe_2TiO_5 photoanode by electrospray and surface F-modification, Nanoscale 10 (2018) 6678–6683.

[4] J.H. Kim, J.S. Lee, $BiVO_4$-Based heterostructured photocatalysts for solar water splitting: a review, Energy Environ. Focus. 3 (2014) 339–353.

[5] G. Seitz, N. Penin, L. Decoux, A. Wattiaux, M. Duttine, M. Gaudon, Near the ferric pseudobrookite composition (Fe_2TiO_5), Inorg. Chem. 55 (2016) 2499–2507.

[6] M. Dondi, F. Matteucci, G. Cruciani, G. Gasparotto, D.M. Tobaldi, Pseudobrookite ceramic pigments: crystal structural, optical and technological properties, Solid State Sci. 9 (2007) 362–369.

[7] M.V. Nikolic, M.D. Lukovic, Z.Z. Vasiljevic, N.J. Labus, O.S. Aleksic, Humidity sensing potential of Fe_2TiO_5—pseudobrookite, J. Mater. Sci. Mater. Electron. 29 (2018) 9227–9238.

[8] C. Chen, F. Giovannelli, F. Delorme, Thermoelectric properties of $Fe_{2-x}Ti_{1+x}O_5$ solid solutions: influence of microcracking and Nb substitution, Ceram. Int. 44 (2018) 21794–21799.

[9] S. Sharma, T. Basu, A. Shahee, K. Singh, N.P. Lalla, E.V. Sampathkumaran, Multiglass properties and magnetoelectric coupling in the uniaxial anisotropic spin-cluster-glass Fe_2TiO_5, Phys. Rev. B 90 (2014) 144426.

[10] U. Atzmony, E. Gurewitz, M. Melamud, H. Pinto, H. Shaked, G. Gorodetsky, et al., Anisotropic spin-glass behavior in Fe_2TiO_5, Phys. Rev. Lett. 43 (1979) 782–785.

[11] K. Binder, A.P. Young, Spin glasses: experimental facts, theoretical concepts, and open questions, Rev. Mod. Phys. 58 (1986) 801–976.

[12] W.Q. Guo, S. Malus, D.H. Ryan, Z. Altounian, Crystal structure and cation distributions in the $FeTi_2O_5$ -Fe_2TiO_5 solid solution series, J. Phys. Condens. Matter 11 (1999) 6337–6346.

[13] E. Gurewitz, U. Atzmony, Mössbauer-effect study of Fe_2TiO_5, an anisotropic uniaxial spin-glass, Phys. Rev. B 26 (1982) 6093–6098.

[14] Y. Yeshurun, H. Sompolinsky, Transverse ordering in anisotropic spin glasses, Phys. Rev. B 31 (1985) 3191–3193.

[15] S. Sharma, T. Basu, A. Shahee, K. Singh, N.P. Lalla, E.V. Sampathkumaran, Complex dielectric and impedance behavior of magnetoelectric Fe_2TiO_5, J. Alloys Compd. 663 (2016) 289–294.

[16] E. Granado, J.A. Sanjurjo, C. Rettori, J.J. Neumeier, S.B. Oseroff, Order-disorder in the Jahn-Teller transition of $LaMnO_3$: a Raman scattering study, Phys. Rev. B Condens. Matter Mater. Phys. 62 (2000) 11304–11307.

[17] R.B. Macedo Filho, A. Pedro Ayala, C. William de Araujo Paschoal, Spin-phonon coupling in Y_2NiMnO_6 double perovskite probed by Raman spectroscopy, Appl. Phys. Lett. 102 (2013) 192902.

[18] W.S. Ferreira, J. Agostinho Moreira, A. Almeida, M.R. Chaves, J.P. Araújo, J.B. Oliveira, et al., Spin-phonon coupling and magnetoelectric properties: $EuMnO_3$ versus $GdMnO_3$, Phys. Rev. B 79 (2009) 54303.

[19] J. Laverdière, S. Jandl, A.A. Mukhin, V.Y. Ivanov, V.G. Ivanov, M.N. Iliev, Spin-phonon coupling in orthorhombic $RMnO_3$ (R = Pr, Nd, Sm, Eu, Gd, Tb, Dy, Ho, Y): a Raman study, Phys. Rev. B Condens. Matter Mater. Phys. 73 (2006) 1–5.

[20] W. Baltensperger, J.S. Helman, Influence of magnetic order in insulators on the optical phonon frequency, Helv. Phys. Acta 41 (1968) 668–673.

[21] M.G. Cottam, D.J. Lockwood, Spin-phonon interaction in transition-metal difluoride antiferromagnets: theory and experiment, Low Temp. Phys. 45 (2019) 78–91.

[22] R. Vilarinho, E.C. Queirós, A. Almeida, P.B. Tavares, M. Guennou, J. Kreisel, et al., Scaling spin–phonon and spin–spin interactions in magnetoelectric $Gd_{1-x}Y_xMnO_3$, J. Solid State Chem. 228 (2015) 76–81.

[23] Y. Yamaguchi, T. Kimura, Magnetoelectric control of frozen state in a toroidal glass, Nat. Commun. 4 (2013) 1–5.

[24] D.A.B. Barbosa, C.W.A. Paschoal, Raman evidence for presence of high-temperature ferromagnetic clusters in magnetodielectric compound Ba-doped La_2NiMnO_6, Spectrochim. Acta Part A Mol. Biomol. Spectrosc. 185 (2017) 125–129.

[25] K.R. Chakraborty, B. Paul, R. Shukla, P.S.R. Krishna, A. Kumar, M.D. Mukadam, et al., Revealing magnetic ordering and spin-phonon coupling in $Y_{1-x}Tb_xMnO_3$ ($0.1 \leq x \leq 0.3$) compounds, J. Phys. Condens. Matter 29 (2017) 155804.

[26] J.S. Lee, T.W. Noh, J.S. Bae, I.-S. Yang, T. Takeda, R. Kanno, Strong spin-phonon coupling in the geometrically frustrated pyrochlore $Y_2Ru_2O_7$, Phys. Rev. B 69 (2004) 214428.

[27] A. Milosavljević, A. Šolajić, J. Pešić, Y. Liu, C. Petrovic, N. Lazarević, et al., Evidence of spin-phonon coupling in $CrSiTe_3$, Phys. Rev. B 98 (2018) 104306.

[28] V.V. Shvartsman, S. Bedanta, P. Borisov, W. Kleemann, A. Tkach, P.M. Vilarinho, (Sr,Mn)TiO_3: A magnetoelectric multiglass, Phys. Rev. Lett. 101 (2008) 17–20.

[29] J. Rodríguez-Carvajal, Recent advances in magnetic structure determination by neutron powder diffraction, Phys. B Phys. Condens. Matter. 192 (1993) 55–69.

[30] B. Ravel, M. Newville, ATHENA, ARTEMIS, HEPHAESTUS: data analysis for X-ray absorption spectroscopy using IFEFFIT, J. Synchrotron Radiat. 12 (2005) 537–541.

[31] D.A. Long, The Raman Effect: A Unified Treatment of the Theory of Raman Scattering by Molecules, John Wiley & Sons, West Sussex, England, 2002.

[32] R. Demichelis, B. Civalleri, M. Ferrabone, R. Dovesi, On the performance of eleven DFT functionals in the description of the vibrational properties of aluminosilicates, Int. J. Quantum Chem. 110 (2010) 406–415.

[33] R. Dovesi, A. Erba, R. Orlando, C.M. Zicovich-Wilson, B. Civalleri, L. Maschio, et al., Quantum-mechanical condensed matter simulations with *CRYSTAL*, Wiley Interdiscip. Rev. Comput. Mol. Sci. 8 (2018), e1360.

[34] M. Catti, G. Valerio, R. Dovesi, Theoretical study of electronic, magnetic, and structural properties of α-Fe_2O_3 (hematite), Phys. Rev. B 51 (1995) 7441–7450.

[35] G. Sophia, P. Baranek, C. Sarrazin, M. Rérat, R. Dovesi, First-principles study of the mechanisms of the pressure-induced dielectric anomalies in ferroelectric perovskites, Phase Transitions 86 (2013) 1069–1084.

[36] L. Maschio, B. Kirtman, R. Orlando, M. Rèrat, Ab initio analytical infrared intensities for periodic systems through a coupled perturbed Hartree-Fock/Kohn-Sham method, J. Chem. Phys. 137 (2012) 204113.

[37] L. Maschio, B. Kirtman, M. Rérat, R. Orlando, R. Dovesi, Ab initio analytical Raman intensities for periodic systems through a coupled perturbed Hartree-Fock/Kohn-Sham method in an atomic orbital basis. II. Validation and comparison with experiments, J. Chem. Phys. 139 (2013) 164102.

[38] L. Pauling, VII. The crystal structure of pseudobrookite, Z. für Kristallogr. Cryst. Mater. 73 (1930) 97–112.

[39] K. Srivastava, W. Treutmann, E. Untersteller, Anisotropic spin glass pseudobrookite: Evidence for transverse freezing and possible implications, Phys. Rev. B Condens. Matter Mater. Phys. 68 (2003) 1–6.

[40] F. Liu, H. He, L. Xie, XAFS study on the specific deoxidation behavior of iron titanate catalyst for the selective catalytic reduction of NO_x with NH_3, ChemCatChem 5 (2013) 3760–3769.

[41] T. Yamashita, P. Hayes, Analysis of XPS spectra of Fe^{2+} and Fe^{3+} ions in oxide materials, Appl. Surf. Sci. 254 (2008) 2441–2449.

[42] J.K. Srivastava, J. Hammann, Anisotropic spin glass behavior of Mn^{3+} : Fe_2TiO_5 system, Jpn. J. Appl. Phys. 26 (1987) 789.

[43] T. Ohsaka, F. Izumi, Y. Fujiki, Raman spectrum of anatase, TiO_2, J. Raman Spectrosc. 7 (1978) 321–324.

[44] P.S. Narayanan, Raman spectrum of rutile (TiO_2), Proc. Indian Acad. Sci. (Math. Sci.) (1950) 279–283.

[45] O. Frank, M. Zukalova, B. Laskova, J. Kürti, J. Koltai, L. Kavan, Raman spectra of titanium dioxide (anatase, rutile) with identified oxygen isotopes (16, 17, 18), Phys. Chem. Chem. Phys. 14 (2012) 14567–14572.

[46] D.L.A. de Faria, S. Venâncio Silva, M.T. de Oliveira, Raman microspectroscopy of some iron oxides and oxyhydroxides, J. Raman Spectrosc. 28 (1997) 873–878.

[47] D. Bersani, P.P. Lottici, A. Montenero, Micro-Raman study of iron-titanium oxides obtained by sol-gel synthesis, J. Mater. Sci. 35 (2000) 4301–4305.

[48] T. Wang, C. Sanchez, J. Groenen, P. Sciau, Raman spectroscopy analysis of terra sigillata: the yellow pigment of marbled sigillata, J. Raman Spectrosc. 47 (2016) 1522–1527.

[49] M. He, B. Winkler, J.D. Bauer, L. Bayarjargal, J. Ruiz-Fuertes, I. Alencar, et al., Lattice dynamics and Mg/Ti order in orthorhombic pseudobrookite-type $MgTi_2O_5$, J. Alloys Compd. 699 (2017) 16–24.

[50] M. Balkanski, R. Wallis, E. Haro, Anharmonic effects in light scattering due to optical phonons in silicon, Phys. Rev. B 28 (1983) 1928–1934.

[51] V. Srinu Bhadram, B. Rajeswaran, A. Sundaresan, C. Narayana, Spin-phonon coupling in multiferroic $RCrO_3$ (R-Y, Lu, Gd, Eu, Sm): a Raman study, EPL Europhys. Lett. 101 (2013) 17008.

[52] A. Nonato, B.S. Araujo, A.P. Ayala, A.P. Maciel, S. Yanez-Vilar, M. Sanchez-Andujar, et al., Spin-phonon and magnetostriction phenomena in $CaMn_7O_{12}$ helimagnet probed by Raman spectroscopy, Appl. Phys. Lett. 105 (2014) 222902.

[53] J.M.R. Cruz, P.C. Morais, K.S. Neto, On the spin-glass transition in pseudobrookite, Phys. Lett. A 116 (1986) 45–47.

[54] T. Katsufuji, H. Takagi, Coupling between magnetism and dielectric properties in quantum paraelectric $EuTiO_3$, Phys. Rev. B Condens. Matter Mater. Phys. 64 (2001) 3–6.

[55] G. Lawes, A.P. Ramirez, C.M. Varma, M.A. Subramanian, Magnetodielectric effects from spin fluctuations in isostructural ferromagnetic and antiferromagnetic systems, Phys. Rev. Lett. 91 (2003) 1–4.

[56] E. Granado, A. García, J.A. Sanjurjo, C. Rettori, I. Torriani, F. Prado, et al., Magnetic ordering effects in the Raman spectra of $La_{1-x}Mn_{1-x}O_3$, Phys. Rev. B 60 (1999) 11879–11882.

[57] J.A. Moreira, A. Almeida, W.S. Ferreira, J.E. Araújo, A.M. Pereira, M.R. Chaves, et al., Coupling between phonons and magnetic excitations in orthorhombic $Eu_{1-x}Y_xMnO_3$, Phys. Rev. B 81 (2010) 54447.

[58] D.J. Lockwood, M.G. Cottam, The spin-phonon interaction in FeF_2 and MnF_2 studied by Raman spectroscopy, J. Appl. Phys. 64 (1988) 5876–5878.

[59] A. Ayala, C. Paschoal, I. Guedes, W. Paraguassu, P. Freire, J. Mendes Filho, et al., Disorder-induced symmetry lowering in the $CsInMgF_6$ pyrochlore crystal, Phys. Rev. B 66 (2002) 214105.

[60] L. Martín-Carrón, A. De Andrés, M.J. Martínez-Lope, M.T. Casais, J.A. Alonso, Raman phonons as a probe of disorder, fluctuations, and local structure in doped and undoped orthorhombic and rhombohedral manganites, Phys. Rev. B Condens. Matter Mater. Phys. 66 (2002) 1–8.

[61] S. Mahana, B. Rakshit, R. Basu, S. Dhara, B. Joseph, U. Manju, et al., Local inversion symmetry breaking and spin-phonon coupling in the perovskite $GdCrO_3$, Phys. Rev. B 96 (2017) 1–9.

[62] S.P. Marcondes, J.E.F.S. Rodrigues, M.R.B. Andreeta, A.C. Hernandes, Resonance Raman spectroscopy of $NdAlO_3$ single-crystal fibers grown by the laser-heated pedestal growth technique, Vib. Spectrosc. 73 (2014) 144–149.

[63] J.E. Rodrigues, M.M. Ferrer, T.R. Cunha, R.C. Costa, J.R. Sambrano, A.D. Rodrigues, et al., First-principles calculations and Raman scattering evidence for local symmetry lowering in rhombohedral ilmenite: temperature- and pressure-dependent studies, J. Phys. Condens. Matter 30 (2018) 485401.